RSC Advances

PAPER

Cite this: *RSC Adv.*, 2016, **6**, 86101

Shape-selective synthesis of NiO nanostructures for hydrazine oxidation as a nonenzymatic amperometric sensor†

Dhanasekaran Vikraman[a] and Hui Joon Park*[ab]

Received 17th May 2016
Accepted 5th September 2016

DOI: 10.1039/c6ra12805j

www.rsc.org/advances

In this work, we demonstrate the shape-dependent electrocatalytic activity of NiO NPs towards hydrazine oxidation. For this purpose, NiO NPs, having pellet, rod, dot and cuboid-shapes, were synthesized using a variety of reducing agents such as sodium hydroxide (NaOH) with polyethylene glycol (PEG), NaOH without PEG, ammonia (NH_3), and sodium carbonate (Na_2CO_3) *via* a simple and low cost sol–gel approach. Moreover, NiO–silica core–shell (NiO@SiO_2) NPs were prepared using TEOS as a source of the porous silica. The morphological structures of these NPs were characterized by field emission-scanning electron microscopy (FE-SEM) and transmission electron microscopy (TEM). From the X-ray diffraction (XRD) results, a face-centered cubic (fcc) NiO crystalline structure was confirmed and the estimated size of the crystalline NPs was in the range of 2.7–12.5 nm depending on the reducing agents utilized for the synthesis. Moreover, their characteristics were further investigated by Raman spectroscopy. From the cyclic voltammetry results, it was shown that the nano-pellet shape NiO exhibited the best electrocatalytic performance for hydrazine oxidation and stability, promising for fuel cell application.

1. Introduction

The design and fabrication of nanostructure-based materials have been core research topics due to their unique properties in the nanoscale, often not presented in the bulk state.[1,2] Particularly, in electrocatalysis,[3] many structure-sensitive catalytic reactions have been reported, and their electrochemical reactivity on the surface of the structure has been extensively investigated to utilize them to design new electrocatalytic material systems. Nanoparticle (NP)-based system is a representative example, of which its catalytic properties can be tuned by controlling its atomic composition, crystallinity, size and morphology.[4,5] For instance, NPs having similar size and composition but different surface nature, usually originated from the different synthesis routes, can often exhibit different electrocatalytic properties, and various shape-oriented catalytic properties of NPs, additionally added to their physicochemical and electronic properties, have been reported.[6,7]

Hydrazine and its derivatives are widely used in chemical industry as a precursor to blowing agent, fuel cell, heat stabilizer, and rocket fuel.[8,9] In particular, carbon free hydrazine liquid is one of the promising candidates for the fuel cell because of their high theoretical cell voltage (1.61 V) and hydrogen content, power density, and easy transportation and storage without any greenhouse gas emission.[10] As a direct liquid fuel cell system, electro-oxidation of fuel process does not suffer from any poisoning effects and there are no CO-like intermediate poisoning species.[11,12]

Various nanostructured electrode materials, such as noble metal nanoparticles,[13–15] redox mediators,[15–17] graphene,[18] and metal oxides,[19,20] were developed as electrocatalysts for hydrazine oxidation. The noble metals exhibit high electrocatalytic activities, however, the high cost and scarcity limit their utilization as electrode materials in fuel cell at a large scale. Therefore, considerable interests have been concentrated on developing cheap and sustainable noble metal-free electrocatalysts for the hydrazine oxidation. Transition metal oxides such as NiO, TiO_2, ZnO, CuO, SnO_2, and WO_3 are extremely attractive as catalysts owing to their extraordinarily catalytic activities for oxidation reactions.[21–25] Especially, NiO-based nanomaterials having a band gap from 3.6 to 4.0 eV have been widely studied for fuel cell electrodes,[1,26–30] due to its unique electrical, optical and magnetic properties.[31,32] To synthesize those NiO nanostructures, various methods including co-precipitation, sol–gel, thermal decomposition, and hydrothermal have developed.[33–35]

In this work, we report NiO NP-shape/size dependent electrocatalytic oxidation of hydrazine. The shape and size of NiO NPs were tuned by changing the reducing agents during their

[a]*Division of Energy Systems Research, Ajou University, Suwon 16499, Republic of Korea. E-mail: huijoon@ajou.ac.kr*

[b]*Department of Electrical and Computer Engineering, Ajou University, Suwon 16499, Republic of Korea*

† Electronic supplementary information (ESI) available. See DOI: 10.1039/c6ra12805j

synthesis. Using transmission electron microscopy (TEM) and scanning electron microscopy (SEM), the shape and size variations of NiO NPs were investigated and their characteristics were analyzed by X-ray diffraction (XRD) and Raman scattering. Furthermore, core–shell type NiO–SiO_2 NPs were synthesized and their electrocatalytic activities were analyzed.

2. Experimental

2.1. Preparation of NiO nanostructure

The NiO nanostructures were prepared by chemical co-precipitation method. For NiO preparation, 0.25 M nickel nitrate ($Ni(NO_3)_2$) was used as a source material. In this case, three different reducing agents were used for preparation of NiO NPs such as sodium hydroxide (NaOH), ammonia (NH_3) and sodium carbonate (Na_2CO_3). Firstly, 1 M NaOH solution was added by drop wise (2 ml min^{-1}) into 0.25 M $Ni(NO_3)_2$ solution. The mixed solution was vigorously stirred for 4 hours. Solution bath temperatures were varied from 40 to 85 °C. After continuous stirring, 100 ml deionized water was added to the solution and then it was subjected to refluxing process for 2 hours at 300 °C. The collected material was then washed several times with deionized water and ethanol, and it was dried at 100 °C for 6 hours. The final product was calcined in air at 350 °C for 2 hours. The same procedure was continued using NH_3 and Na_2CO_3 instead of NaOH. Polyethylene glycol (PEG – average MW = 2000) was used as a surfactant to reduce the agglomeration of NPs. To prepare sample using NaOH with PEG, PEG-dissolved deionized water was added by drop wise to 0.25 M $Ni(NO_3)_2$ solution and then the above mentioned procedure was employed.

2.2. Preparation of NiO@SiO_2 nanostructure

The core–shell NiO@SiO_2 samples were prepared by a modified Stöber method. Briefly, 0.5 g of polyvinylpyrrolidone (PVP) was added to deionized water at room temperature. After 20 minutes continuous stirring, 0.1 g of as-prepared NiO nanostructures were mixed with PVP solution. After stirring for 12 hours, 10 ml of NH_3 (28 wt%) was added and then the suspension was sonicated for 30 min in a sonicator. Subsequently, 0.5 ml of tetraethyl orthosilicate (TEOS)-mixed solution was injected into the suspension. The product was collected after 2 hours centrifugation, washed twice with distilled water and ethanol, and dried at 100 °C in air for 6 hours. The core–shell samples having NiO cores were subjected to calcination at 500 °C for 2 hours. The samples are designated by its reducing agent such as NaOH with PEG, NaOH w/o PEG, NH_3 and Na_2CO_3. The representation of preparation methods for NiO and their core–shell structures are given in Scheme 1.

2.3. Preparation of Nafion/NiO/GC electrode

Glassy carbon electrodes (GCE, 3 mm-diameter) were polished with alumina slurry. After rinsing thoroughly with doubly distilled water, they were sonicated in absolute ethanol and doubly distilled water for about 1 minute, respectively. A GCE was loaded with 1 μl of the prepared NiO solution and allowed to dry at ambient temperature. Finally, the electrode was capped with 0.5% Nafion solution (Sigma Aldrich) to protect the active material. The final electrode is taken as the Nafion/NiO/GC electrode. The similar procedures were employed to fabricate the Nafion/NiO@SiO_2/GC electrode.

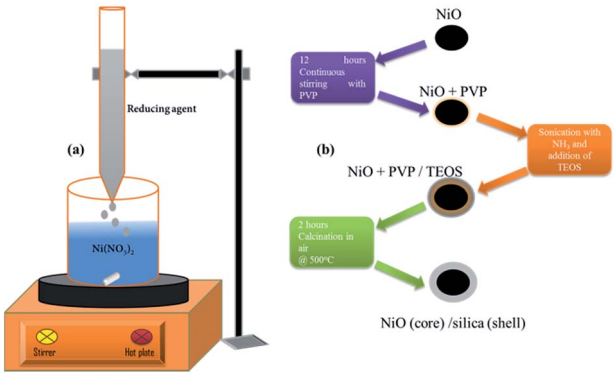

Scheme 1 Schematic representation of (a) NiO nanostructures preparation and (b) their core–shell formation.

2.4. Characterization

X-ray diffraction (XRD) measurements were performed on a Rigaku D/max-2500 diffractometer, using Cu-K_α radiation as the X-ray source in the range of 10–90 °C. Surface morphological properties were analyzed using JEOL JSM-6700F, Japan, field emission scanning electron microscopy (FE-SEM). The shape and size of NiO and NiO@SiO_2 were observed using a FEI Tecnai G2 F30 S-Twin field emission transmission electron microscope (FE-TEM). Synthesized nanostrutures were analyzed by Raman spectroscopy (Renishaw invia RE04, 512 nm Ar laser) with a spot size of 1 μm and scan speed of 30 seconds. Electrochemical measurements of nanostructures were performed on an Ivium electrochemical workstation. The BET surface area measurements were performed using nitrogen adsorption/desorption isotherms with a micromeritics ASAP 2020 physisorption instrument. Three types of electrode configurations were employed. The modified GC electrode was served as a working electrode, whereas an Ag/AgCl (in saturated KCl solution) and a platinum mesh were served as the reference and counter electrodes, respectively.

3. Results and discussion

The structural characteristics of NiO nanostructures were studied by SEM (Fig. 1) and TEM (Fig. 2) images. All the SEM and TEM images correspond to the uniformly distributed NiO NPs having different shapes wherein the identical sizes of a particular morphology are observed. From those images, it was proved that tuning the shape and size of individual NiO NP was possible using different reducing agents. As shown in previous studies,[3,36,37] controlling the shape and size of NP is a prerequisite to provide a particular surface property. NiO NPs, prepared by NaOH with PEG, had a uniform agglomeration nature as shown in SEM image (Fig. 1a). Their individual shape

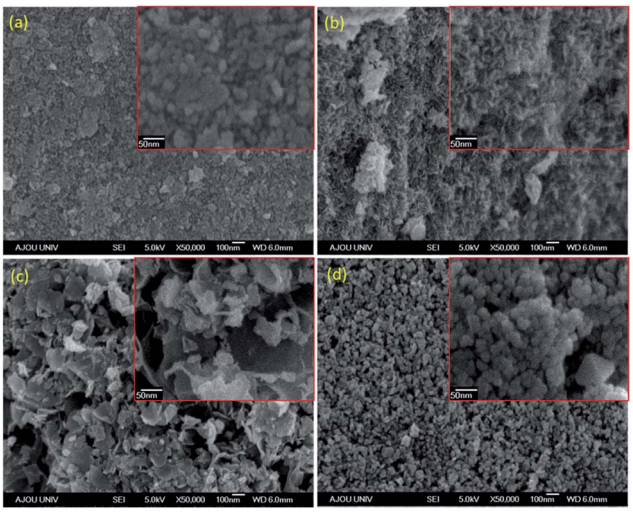

Fig. 1 SEM micrographs of NiO nanostructures prepared using different reducing agents (a) NaOH with PEG, (b) NaOH without PEG, (c) NH_3 and (d) Na_2CO_3. The right inset is high magnification image. All NiO NPs were synthesized at 70 °C.

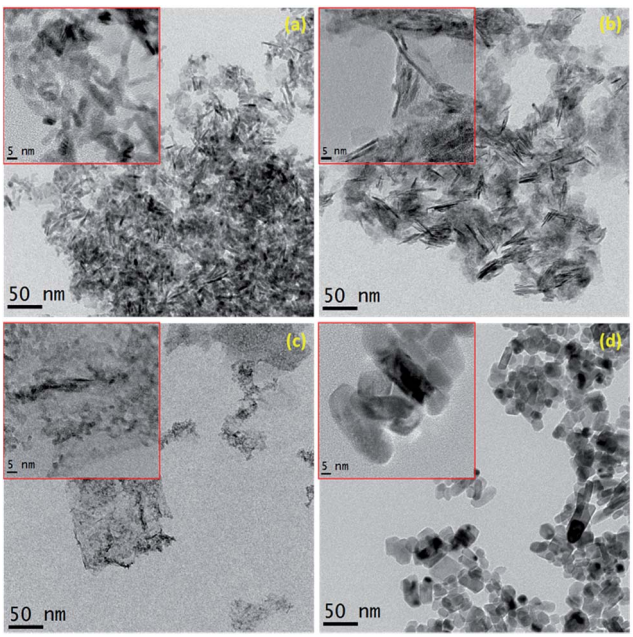

Fig. 2 TEM images of NiO nanostructures prepared using different reducing agents (a) NaOH with PEG, (b) NaOH without PEG, (c) NH_3 and (d) Na_2CO_3. The left inset image represents higher magnification TEM image. All NiO NPs were synthesized at 70 °C.

was identified as a nano-pellet by TEM image and the estimated width was ~3–4 nm (Fig. 2a). NiO NPs, prepared without PEG, showed a nano-rod-shape in both SEM (Fig. 1b) and TEM (Fig. 2b) images, of which the average width slightly decreased to ~2–3 nm, estimated by TEM image (Fig. 2b). Some region of SEM image represented cauliflower-like morphologies, which consisted of rod shape of NiO NPs (Fig. 1b). Flower- or leaf-like morphology was observed for NiO, reduced using NH_3, by SEM (Fig. 1c) and the shape of individual NP was confirmed as nano-dot by TEM (Fig. 2c), which was similar to conventional quantum dot (QD).[38] As for the NiO, prepared with a reducing agent, Na_2CO_3, the cuboid-shaped NPs having the largest size (10–20 nm) were confirmed by both SEM (Fig. 1d) and TEM (Fig. 2d), and the SEM image in Fig. 1d showed that each grain was individually occupied in the NiO without any agglomeration. The shape and size of NiO nanostructures are summarized in Table S1,† including the estimated crystal dimension by XRD, which will be discussed later. The SAED patterns of the corresponding shapes of NiO are given in Fig. S1.† All these NiO NPs were synthesized at 70 °C, and the morphology variation according to the temperature will be discussed later. Consequently, different electrocatalytic activity is expected among these samples as a consequence of their different surface structure.

NiO NPs were further encapsulated by SiO_2 using PVP as a coupling agent.[39,40] SEM and TEM images of SiO_2-encapsulated NiO nanostructures (NiO@SiO_2) are shown in Fig. 3 and S2,† respectively. The amphiphilic and nonionic PVP polymer could be adsorbed onto the colloidal NiO NPs, and then the stabilized colloidal NPs were transferred into an ammonia solution, in which homogeneous silica shells of variable thickness could be directly coated using TEOS as the Si source.[39] The specific surface area and pore size distributions of the NiO@SiO_2 core–shell structures were characterized using nitrogen gas sorption through BET. The surface area of the core–shell structure having cuboid shape NiO, reduced by Na_2CO_3, was evaluated at 47.3 $m^2\ g^{-1}$. The specific surface areas were estimated at 19.3, 22.5 and 32.7 $m^2\ g^{-1}$ for core–shell structures having nano-pellet, nano-rods and nano-dots shapes, respectively. In Table S2,† the BET surface area and pore volume of the NiO@SiO_2 samples according to the different NiO nanostructures are provided. As shown in Fig. S3,† the presence of mesopores in the silica shells is confirmed for cuboid shape NiO@SiO_2. The pore size ranges from 2 to 20 nm, peaking at 9

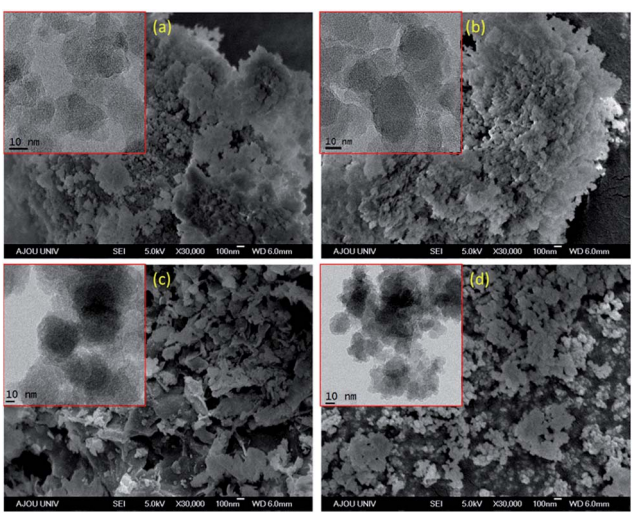

Fig. 3 SEM micrographs of NiO-silica core–shell nanostructures prepared using different reducing agents (a) NaOH with PEG, (b) NaOH without PEG, (c) NH_3 and (d) Na_2CO_3. Insets are corresponding TEM images of NiO-silica core–shell nanostructures.

nm. The mesopores with pore sizes of 3–4 nm SiO_2 shells were developed due to the templating effect of PVP.[41,42]

Structural properties of NiO and NiO@SiO_2 nanostructures were investigated by XRD using CuK_α radiation with $\lambda = 0.154$ nm. XRD patterns of NiO NPs, synthesized by different reducing agents such as NaOH with PEG, NaOH w/o PEG, NH_3 and Na_2CO_3 are shown in Fig. 4a. All the XRD patterns could be indexed with standard diffraction patterns of NiO (JCPDS card no. # 89-7130), and the cubic crystal structure (unit cell parameter $a \sim 4.19$ Å) was confirmed. The preferential orientation along (200) lattice plane was exhibited by NiO NPs regardless of reducing agents. As for NiO, reduced using NaOH with PEG, the calculated d-spacing value of (200) plane was at 2.094 Å, and the diffraction peaks (2θ) were observed at 37.06°, 43.06° and 62.60° corresponding to (111), (200) and (220) lattice planes, respectively. As for NiO, prepared by other reducing agents, the peak positions were almost similar, and no other new peaks from different NiO phase and impurities were shown. The full width at half maximum (FWHM) value of the predominant orientation peak of NiO, reduced using NaOH with PEG was 1.83° and that of NiO, reduced using NH_3, was the maximum observed at 3.15°. From the reflection peak width of XRD data, the crystal size of NiO nanostructures (D) was determined by the Debye–Scherrer's relation using eqn (1);[43]

$$D = K\lambda/\beta \cos\theta \quad (1)$$

where λ is the X-ray wavelength and K is the particle shape factor, taken as 1 in all cases. β is defined as the line-broadening at half-maximum of the peak (FWHM) after subtracting the instrumental line broadening, and θ is the position (angle) of the peak. For these calculations, the (200) peak has been used. The estimated values of crystallite size are 4.66, 3.08, 2.71 and 12.51 nm for NiO reduced using NaOH with PEG, NaOH w/o PEG, NH_3 and Na_2CO_3, respectively, and these results are in good agreement with the TEM characterization results. The crystal structures of NiO@SiO_2 core–shells were also characterized by XRD, and no dramatic changes in crystal structure occurred after encapsulation process. As shown in Fig. 4b, after encapsulation, no noticeable changes in peak position and preferential orientation of NiO were found, and the estimated crystal sizes of NiO NPs were not significantly changed (NaOH with PEG: from 4.66 to 5.0 nm, NaOH w/o PEG: from 3.08 to 10.10 nm, NH_3: from 2.71 to 2.83 nm, and Na_2CO_3: from 12.51 to 12.80 nm). Even though the estimated crystal size of NiO, prepared by NaOH w/o PEG, increased after encapsulation process, the better crystallinity by estimation does not affect any conclusions here.

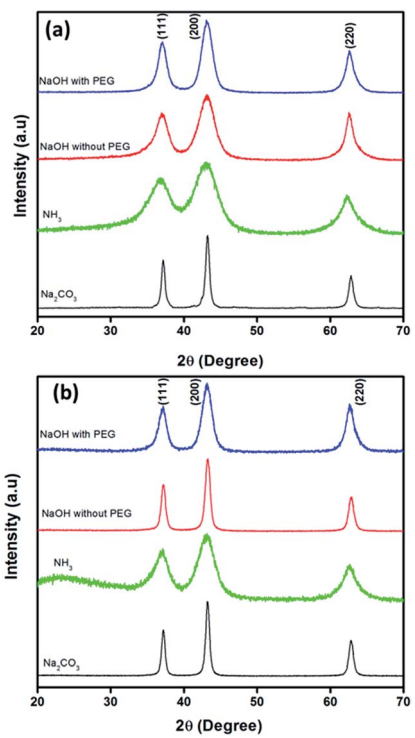

Fig. 4 X-ray diffraction patterns of (a) NiO nanostructures and (b) NiO–silica core–shell nanostructures prepared using different reducing agents.

The morphology of NiO nanostructure was affected by the solution temperature during the synthesis. As a representative, the structure variation of NiO NPs, synthesized by NaOH with PEG, depending on the solution temperature was investigated (Fig. S4 and S5†). The individual shape and size of NP are more discernable in TEM image (Fig. S4†), and the width of nanopellet was shown to decrease as the solution temperature during synthesis increased from 40 to 85 °C. This gradual decrease of the crystal size is also confirmed by XRD in Fig. S6,† and the crystal sizes of NiO, estimated by eqn (1), are 8.06, 6.52, 4.66 and 3.76 nm for 40, 55, 70 and 85 °C conditions, respectively. We believe that more collision between crystallites in the solution at higher bath temperature leads to the formation of smaller size grain during the growth of the nanostructure. NiO NPs mostly existed as irregular shaped-agglomerate between 40 and 70 °C and turned to plate or needle-like morphology at 85 °C, maybe due to their smallest crystal domain, as shown in SEM image (Fig. S5†). Even though the morphology and crystal dimension of NiO NP were affected by the solution temperature, it was confirmed by XRD measurements that the NiO remains as cubic structures with similar preferential orientation and no other phase or impurity were generated (Fig. S6†).

Raman spectroscopy, which is a sensitive probe to the local atomic arrangements and vibrations, has been widely used to investigate the microstructural nature of the nanosized material.[44,45] The presence of NiO was confirmed by Raman scattering spectra, which provided the Raman stretching mode, in Fig. 5. Raman spectra obviously represented the solely exhibited Ni–O related peak at 503 cm^{-1}.[46,47]

The oxidation of hydrazine at Nafion/NiO/GC can be expressed as the following reaction:[48]

$$N_2H_5^+ \rightarrow N_2 + 5H^+ + 4e^- \quad (2)$$

When the pH values are less than the pK_a of protonated hydrazine (pK_a $N_2H_5^+ = 8.1$), hydrazine is positively charged, which induces a repulsive force with the surface of electrode during the anodic change of potential.[49,50] This mechanism

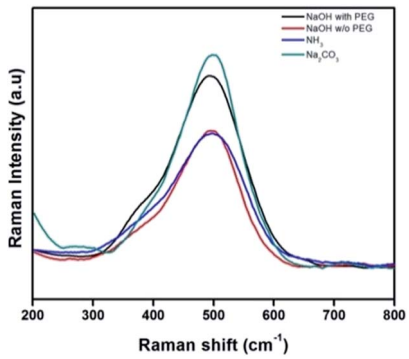

Fig. 5 Raman scattering of NiO nanostructures prepared by the different reducing agents.

explains the irreversibility of the reaction and the absence of the cathodic peak because of the formation of stable species such as nitrogen as an end product. Meanwhile, SEM images of Nafion/NiO/GC and Nafion/NiO@SiO_2/GC electrode surfaces according to the different NiO structures are shown in Fig. S7 and S8,† respectively. These images proved the uniformity of the surface of electrode without any voids. The cyclic voltammograms (CVs) of Nafion/NiO/GC electrode in 0.025 M NaOH with 0.1 M hydrazine at 100 mV s^{-1} scan rate is shown in Fig. 6a. As for nano-dot-shaped NiO NPs (from NH_3)-based Nafion/NiO/GC electrode, the peak potential is noticed at −0.14 V *vs.* Ag/AgCl and the catalytic activity is at 310 mA g^{-1}. For the nano-rod-shaped NiO NPs (from NaOH w/o PEG)-based Nafion/NiO/GC electrode, the peak potential is −0.20 V and the catalytic activity increases to 396 mA g^{-1}. In the case of cuboid-shaped NiO NPs (from Na_2CO_3), the peak potential is observed at −0.15 V, which gets further shifted toward more positive values than that of nano-dot-shaped NiO NP-based Nafion/NiO/GC electrode, and the catalytic activity also increases by almost twice (503 mA g^{-1}), compared to that of nano-dot-based one (Fig. 6a). Finally, nano-pellet-shaped NiO NP (from NaOH with PEG)-based Nafion/NiO/GC electrode exhibits the highest electrocatalytic activity (953 mA g^{-1}), which indicates the obvious advantage of this shape of NiO NP (*e.g.* larger active area) for electro-oxidation. In this case, an oxidation peak is observed at −0.1 V *vs.* Ag/AgCl. Compared with other shaped NP, the pellet geometries have an obvious influence on the electrocatalytic activity of NiO NP because of their active crystalline planes, large surface area to volume ratio and curvature-induced charge density at the apex of NPs.[51] Moreover, NaOH with PEG highly protects their pellet shape formation, compared with other reducing agents yielding the shapes.[39] Consequently, the electrocatalytic activity of Nafion/NiO/GC electrode is highly dependent on the morphological nature of as-synthesized NiO nanostructures.[52]

As a comparison, the electrocatalytic activity of Nafion/NiO@SiO_2/GC electrode towards hydrazine oxidation was also investigated using CVs. Fig. 7a depicts that CVs of Nafion/NiO@SiO_2/GC electrode in 0.025 M NaOH with 0.1 M hydrazine at 100 mV s^{-1} scan rate. Overall, the catalytic activities were reduced for silica-capped NiO nanostructures. Also, the maximum catalytic activity was exhibited at 325 mA g^{-1} for

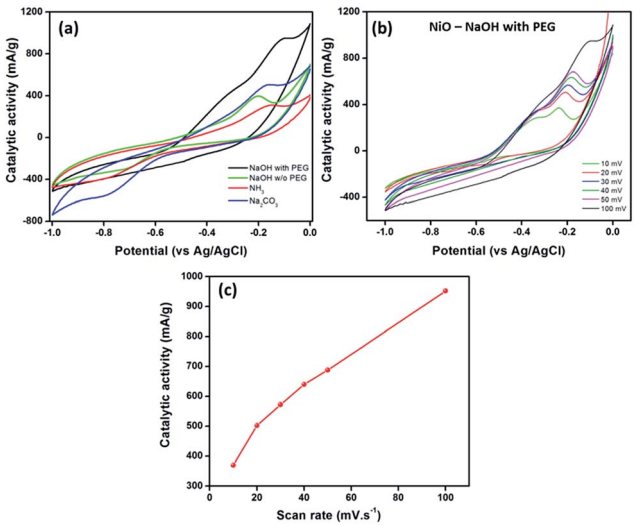

Fig. 6 Hydrazine oxidation performance using electrochemical measurements. (a) Cyclic voltammograms of the Nafion/NiO/GC electrodes (depending on the various types of NiO NPs) in 0.025 M NaOH with 0.1 M hydrazine hydrate at 100 mV s^{-1} scan rate. (b) Cyclic voltammograms of the Nafion/NiO/GC electrode (based on NiO NPs, reduced by NaOH with PEG) in 0.025 M NaOH with 0.1 M hydrazine hydrate at different scan rate such as 10, 20, 30, 40, 50 and 100 mV s^{-1}. (c) Scan rate *vs.* catalytic activity of Nafion/NiO/GC electrode (based on NiO NPs, reduced by NaOH with PEG). Reference electrode: Ag/AgCl and counter electrode: Pt.

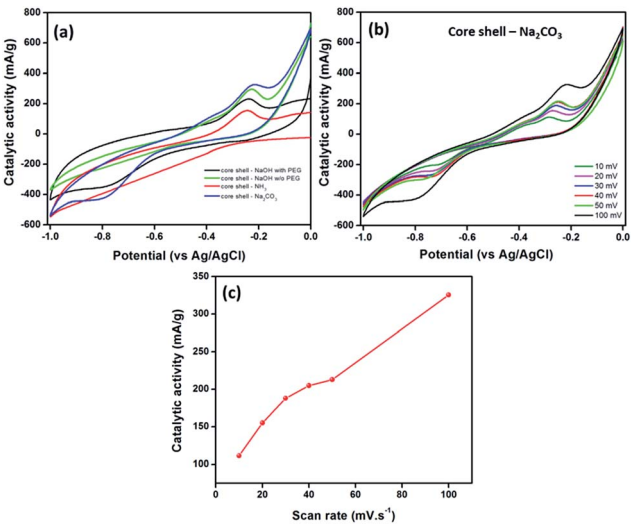

Fig. 7 Hydrazine oxidation performance using electrochemical measurements. (a) Cyclic voltammograms of the Nafion/NiO@SiO_2/GC electrode (depending on the various types of NiO@SiO_2 NPs) in 0.025 M NaOH with 0.1 M hydrazine hydrate at 100 mV s^{-1} scan rate. (b) Cyclic voltammograms of the Nafion/NiO@SiO_2/GC electrode (based on NiO NPs, reduced by Na_2CO_3) in 0.025 M NaOH with 0.1 M hydrazine hydrate at different scan rate such as 10, 20, 30, 40, 50 and 100 mV s^{-1}. (c) Scan rate *vs.* catalytic activity of Nafion/NiO/GC electrode (based on NiO NPs, reduced by Na_2CO_3). Reference electrode: Ag/AgCl and counter electrode: Pt.

cuboid-shaped NiO–silica core–shell NPs, which is 64% of the catalytic activity of as-synthesized NiO. The electrocatalytic activities of remaining NiO@SiO_2 were observed at 231, 298 and 155 mA g^{-1}, which corresponded to nano-pellets, nano-rods and nano-dots, respectively. Consequently, it has been concluded that the individual electrocatalytic property of NiO was suppressed by the SiO_2 shell structures. The electrocatalytic activity values according to the shape of NiO NP are summarized in Table S3.†

CV measurements at different scan rates were performed to investigate the reaction mechanism of hydrazine oxidation for the NiO nanostructure-based electrodes. Fig. 6b represents the CV curves of Nafion/NiO (reduced by NaOH with PEG)/GC at different scan rates from 10 to 100 mV s^{-1}, which indicates that the oxidation peak potential and the catalytic mass activity increase with the scan rate. Nafion/NiO (reduced by NaOH with PEG)/GC electrode, which showed the best performances, was selected as a representative. This linear dependence of the catalytic activity *vs.* the scan rate (Fig. 6c) indicates that the electrochemical oxidation of hydrazine on this Nafion/NiO/GC electrode is a typical adsorption-limited process and our electrodes have the uniform quality. The similar relation between the catalytic activity and the scan rate was also observed from Nafion/NiO@SiO_2/GC electrode. As shown in Fig. 7b and c, the catalytic activity of Nafion/NiO@SiO_2/GC electrode, based on cuboid-shaped NiO showing the best performance, was linear to the scan rate. Meanwhile, in Fig. S9,† the CV curves of Nafion/NiO/GC electrode using NaOH electrolyte with and without hydrazine confirmed the hydrazine oxidation. To the best of our knowledge, this is the first report, which studies the shape-dependent electrocatalytic hydrazine oxidation of various types of NiO NPs and NiO–silica core–shell NPs.

Chronoamperometric measurements were carried out to appraise the durability of the catalysts, because the stability of catalysts is important to the application of fuel cells. Fig. 8a shows the amperometric *i–t* curves of Nafion/NiO/GC electrodes having different shaped NiO. In the initial period, the decay current density decreased rapidly for all the catalysts. This may be due to the formation of the intermediate species during the hydrazine oxidation reaction. However, during the whole time, the catalytic activity of the Nafion/NiO/GC electrode, which comprised nano-pellet-shaped NiO, was larger than other shaped NiO-based Nafion/NiO/GC electrodes. Furthermore, the robustness and chemical stability of the nanostructures reported here are responsible for their stability against electro-oxidation process. Fig. 8b shows the CV results during 100 consecutive cycles about the nano-pellet-shaped NiO-comprised electrode, which prove their stability. Consequently, nano-pellet-shaped NiO NPs was found to exhibit superior electrocatalytic activity compared to the other structures for the electrochemical oxidation of hydrazine.

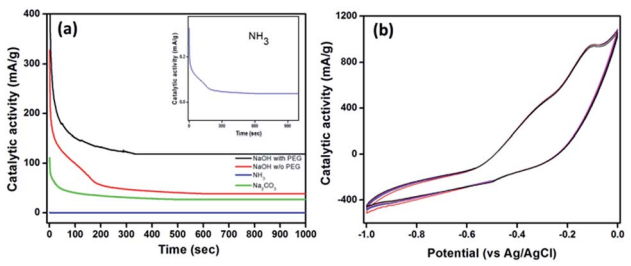

Fig. 8 (a) Chronoamperometric responses of Nafion/NiO/GC electrode (depending on the various types of NiO NPs) in 0.025 M NaOH with 0.1 M hydrazine hydrate. (b) Multiple cycle performance of Nafion/NiO/GC electrode (based on NiO NPs, reduced by NaOH with PEG) at 100 mV s^{-1} scan rate. Reference electrode: Ag/AgCl and counter electrode: Pt.

4. Conclusions

Various shapes of NiO NPs and their silica core–shell structures were prepared by simple chemical strategy. The shape and size variation of NPs were analyzed by TEM and their morphological properties were investigated by SEM. Furthermore, their characteristics including the crystal structure were studied by XRD and Raman spectroscopy. Finally, the electrocatalytic activities of NiO NP-based electrodes were demonstrated by CVs, and their stability was also perceived by amperomertric and multiple cycle performances. The nano-pellet shape NiO exhibited the best electrocatalytic performance of 953 mA g^{-1} for hydrazine oxidation. From our results, it is clearly shown that controlling the shape and size of NP is an effective way to develop highly active electrocatalysts for the fuel cell application.

Acknowledgements

This work is supported by the Basic Science Research Program through the National Research Foundation of Korea (NRF) funded by the Ministry of Education (2014R1A1A2056403). This work was also partially supported by the National Research Foundation (NRF) of Korea (Grant no. 2009-0094046). Authors also acknowledge the support by the Ministry of Trade, Industry & Energy (MOTIE, 10051565) and Korea Display Research Corporation (KDRC) support program for the development of future devices technology for display industry.

Notes and references

1 S. Jana, S. Samai, B. C. Mitra, P. Bera and A. Mondal, *Dalton Trans.*, 2014, **43**, 13096–13104.
2 J. Kong, N. R. Franklin, C. Zhou, M. G. Chapline, S. Peng, K. Cho and H. Dai, *Science*, 2000, **287**, 622–625.
3 J. Solla-Gullon, F. Vidal-Iglesias and J. Feliu, *Annu. Rep. Prog. Chem., Sect. C: Phys. Chem.*, 2011, **107**, 263–297.
4 A. Wieckowski, E. R. Savinova and C. G. Vayenas, *Catalysis and electrocatalysis at nanoparticle surfaces*, CRC Press, 2003.
5 J. Solla-Gullon, F. Vidal-Iglesias, A. Lopez-Cudero, E. Garnier, J. Feliu and A. Aldaz, *Phys. Chem. Chem. Phys.*, 2008, **10**, 3689–3698.
6 B. Beden, J.-M. Léger and C. Lamy, in *Modern aspects of electrochemistry*, Springer, 1992, pp. 97–264.
7 S. Eustis and M. A. El-Sayed, *Chem. Soc. Rev.*, 2006, **35**, 209–217.

8 N. V. Rees and R. G. Compton, *Energy Environ. Sci.*, 2011, **4**, 1255–1260.
9 J. Sanabria-Chinchilla, K. Asazawa, T. Sakamoto, K. Yamada, H. Tanaka and P. Strasser, *J. Am. Chem. Soc.*, 2011, **133**, 5425–5431.
10 Y. Ma, R. Wang, H. Wang, J. Key and S. Ji, *RSC Adv.*, 2015, **5**, 9837–9842.
11 L. Burke and K. O'Dwyer, *Electrochim. Acta*, 1989, **34**, 1659–1664.
12 A. Serov and C. Kwak, *Appl. Catal., B*, 2010, **97**, 1–12.
13 B. K. Jena and C. R. Raj, *J. Phys. Chem. C*, 2007, **111**, 6228–6232.
14 J. Li and X. Lin, *Sens. Actuators, B*, 2007, **126**, 527–535.
15 N. Maleki, A. Safavi, E. Farjami and F. Tajabadi, *Anal. Chim. Acta*, 2008, **611**, 151–155.
16 A. Abbaspour, M. Shamsipur, A. Siroueinejad, R. Kia and P. R. Raithby, *Electrochim. Acta*, 2009, **54**, 2916–2923.
17 L. Zheng and J.-f. Song, *Sens. Actuators, B*, 2009, **135**, 650–655.
18 Y. Wang, Y. Wan and D. Zhang, *Electrochem. Commun.*, 2010, **12**, 187–190.
19 G. Wang, A. Gu, W. Wang, Y. Wei, J. Wu, G. Wang, X. Zhang and B. Fang, *Electrochem. Commun.*, 2009, **11**, 631–634.
20 B. Fang, C. Zhang, W. Zhang and G. Wang, *Electrochim. Acta*, 2009, **55**, 178–182.
21 X. Ren, S. Zhang, C. Li, S. Li, Y. Jia and J.-H. Cho, *Nanoscale Res. Lett.*, 2015, **10**, 1–6.
22 Z. P. Wei, M. Arredondo, H. Y. Peng, Z. Zhang, D. L. Guo, G. Z. Xing, Y. F. Li, L. M. Wong, S. J. Wang and N. Valanoor, *ACS Nano*, 2010, **4**, 4785–4791.
23 J. Polleux, A. Gurlo, N. Barsan, U. Weimar, M. Antonietti and M. Niederberger, *Angew. Chem.*, 2006, **118**, 267–271.
24 L. Francioso, A. Taurino, A. Forleo and P. Siciliano, *Sens. Actuators, B*, 2008, **130**, 70–76.
25 J. Zhang, S. Wang, Y. Wang, M. Xu, H. Xia, S. Zhang, W. Huang, X. Guo and S. Wu, *Sens. Actuators, B*, 2009, **139**, 411–417.
26 J. Wang, L. Wei, L. Zhang, J. Zhang, H. Wei, C. Jiang and Y. Zhang, *J. Mater. Chem.*, 2012, **22**, 20038–20047.
27 J. Wang, F. Yang, X. Wei, Y. Zhang, L. Wei, J. Zhang, Q. Tang, B. Guo and L. Xu, *Phys. Chem. Chem. Phys.*, 2014, **16**, 16711–16718.
28 Y. Wang, J. Zhu, X. Yang, L. Lu and X. Wang, *Thermochim. Acta*, 2005, **437**, 106–109.
29 R. Makkus, K. Hemmes and J. De Wit, *J. Electrochem. Soc.*, 1994, **141**, 3429–3438.
30 M. Ghosh, K. Biswas, A. Sundaresan and C. Rao, *J. Mater. Chem.*, 2006, **16**, 106–111.
31 E. R. Beach, K. Shqau, S. E. Brown, S. J. Rozeveld and P. A. Morris, *Mater. Chem. Phys.*, 2009, **115**, 371–377.
32 K. C. Liu and M. A. Anderson, *J. Electrochem. Soc.*, 1996, **143**, 124–130.
33 P. Poizot, S. Laruelle, S. Grugeon, L. Dupont and J. Tarascon, *Nature*, 2000, **407**, 496–499.
34 X. Wang, J. Song, L. Gao, J. Jin, H. Zheng and Z. Zhang, *Nanotechnology*, 2004, **16**, 37.
35 E. L. Miller and R. E. Rocheleau, *J. Electrochem. Soc.*, 1997, **144**, 3072–3077.
36 H. Erikson, A. Sarapuu, K. Tammeveski, J. Solla-Gullón and J. M. Feliu, *ChemElectroChem*, 2014, **1**, 1338–1347.
37 Z.-Y. Zhou, N. Tian, Z.-Z. Huang, D.-J. Chen and S.-G. Sun, *Faraday Discuss.*, 2009, **140**, 81–92.
38 L. E. Shea-Rohwer, J. E. Martin, X. Cai and D. F. Kelley, *ECS J. Solid State Sci. Technol.*, 2013, **2**, R3112–R3118.
39 L. Li, S. He, Y. Song, J. Zhao, W. Ji and C.-T. Au, *J. Catal.*, 2012, **288**, 54–64.
40 C. Graf, D. L. Vossen, A. Imhof and A. van Blaaderen, *Langmuir*, 2003, **19**, 6693–6700.
41 K.-S. Chou and C.-C. Chen, *Microporous Mesoporous Mater.*, 2007, **98**, 208–213.
42 P. Lakshmanan, M. S. Kim and E. D. Park, *Appl. Catal., A*, 2016, **513**, 98–105.
43 V. Dhanasekaran and T. Mahalingam, *J. Alloys Compd.*, 2012, **539**, 50–56.
44 M. Yoshikawa, Y. Mori, H. Obata, M. Maegawa, G. Katagiri, H. Ishida and A. Ishitani, *Appl. Phys. Lett.*, 1995, **67**, 694–696.
45 J. Zi, H. Büscher, C. Falter, W. Ludwig, K. Zhang and X. Xie, *Appl. Phys. Lett.*, 1996, **69**, 200–202.
46 Y. Luo, Y. Zhou, J. Fu and H.-L. Zhu, *RSC Adv.*, 2014, **4**, 23904–23913.
47 N. Dharmaraj, P. Prabu, S. Nagarajan, C. Kim, J. Park and H. Kim, *Mater. Sci. Eng. B*, 2006, **128**, 111–114.
48 X. Bo, J. Bai, J. Ju and L. Guo, *Anal. Chim. Acta*, 2010, **675**, 29–35.
49 S. Golabi, H. Zare and M. Hamzehloo, *Microchem. J.*, 2001, **69**, 13–23.
50 M. M. Ardakani, P. Rahimi, H. R. Zare and H. Naeimi, *Electrochim. Acta*, 2007, **52**, 6118–6124.
51 D. Mandal, S. Mondal, D. Senapati, B. Satpati and M. V. Sangaranarayanan, *J. Phys. Chem. C*, 2015, **119**, 23103–23112.
52 C. Zhang, S. Y. Hwang and Z. Peng, *J. Mater. Chem. A*, 2013, **1**, 14402–14408.